Magnetic and electron transport properties of Co₂Si nanomagnets

Balamurugan Balasubramanian , ¹,* Tom A. George, ¹ Priyanka Manchanda, ² Rabindra Pahari, ¹ Ahsan Ullah, ¹ Ralph Skomski, ¹ and David J. Sellmyer, ¹,†

¹Nebraska Center for Materials and Nanoscience and Department of Physics and Astronomy, University of Nebraska, Lincoln, Nebraska 68588, USA

²Department of Physics and Astronomy, Howard University, Washington, DC 20059, USA

(Received 20 August 2020; accepted 21 December 2020; published 5 February 2021)

Magnetotransport and ferromagnetism in thin films of Co_2Si nanoclusters are investigated experimentally and theoretically. The nanoclusters are fabricated by an inert-gas condensation-type cluster-deposition method and have an average size of 11.3 nm. Unlike the bulk Co_2Si that exhibits a very weak net magnetic moment only below 10 K, the nanoclusters exhibit room-temperature ferromagnetism with a substantial saturation magnetization. Key features of the system are its closeness to the Stoner transition, magnetic moments induced by spin polarization starting from surface atoms, and nonuniaxial anisotropy associated with the orthorhombic crystal structure of Co_2Si . A method is introduced to determine the effective anisotropy using the experimental magnetization data of this complex system and its relationship with the two lowest-order nonuniaxial anisotropy constants. On decreasing temperature from 300 K, the nanoclusters show electron-transport properties unusual for a ferromagnetic metal, including an increase of Hall resistivity and a nonmonotonic change of negative magnetoresistance with a peak at around 100 K. The underlying physics is explained on the basis of the large polarization of surface spins and variation in the degree of their misalignments due to temperature-dependent effective anisotropy.

DOI: 10.1103/PhysRevMaterials.5.024402

I. INTRODUCTION

Spin-transport properties such as magnetoresistance (MR) and anomalous Hall effect (AHE) in nanostructures have attracted much attention in the context of spintronic devices [1–8]. This includes particulate materials made from magnetic nanoparticles and clusters. Nanoclusters and small nanoparticles exhibit a strong size-dependent modification in electronic structure due to quantum confinement and surface effects and often show entirely different magnetic properties as compared to corresponding bulk materials [9–11]. Thus nanoscale effects are expected to play a crucial role in the electron-transport properties of these structures. Our focus is on nanocluster films of Co₂Si, which is scientifically and technologically an interesting material.

Cobalt-silicon alloys form a rich class of intermetallic compounds with a wide range of electronic and magnetic properties suitable for thermoelectric, nanoelectronics, and spintronics applications [12–18]. Some of these alloys form skyrmionic spin structures associated with Dzyaloshinskii-Moriya interactions and exhibit emerging characteristics like "new-fermion" topological quantum chirality [15,17,18]. Co₂Si is particularly a promising material for interconnects, gates, and source electrodes in integrated devices, and nanoelectronics applications [13,19,20]. An interesting aspect

is that bulk Co₂Si has a very small magnetization of only $41\,\text{emu/cm}^3$ at about 4 K in a field of 70 kOe, corresponding to 0.07 μ_B per Co atom [21,22]. Co₂Si nanowires having diameters between 30 and 80 nm are weakly magnetic but only at temperatures below 50 K [20]. Recently, we have achieved room-temperature ferromagnetism in Co₂Si nanoclusters having sizes in the range of about 10 nm, accompanied by an enhancement of the magnetization by two orders of magnitude as compared to the bulk alloy [22].

Co₂Si nanoclusters exhibit three important features. First, the cluster size is smaller than or comparable to the bulk mean-free path, so that scattering at the clusters' surfaces and contact points becomes an important consideration for electron transport. Second, the magnetism in the bulk Co₂Si is close to a border between the exchange-enhanced Pauli paramagnetism and very weak itinerant ferromagnetism [22], nearly satisfying the Stoner criterion [23,24] and therefore close to ferromagnetism. Existing magnetic moments, associated for example with impurities and surface atoms in this class of systems, easily spin polarize the material, and the size $1/\kappa$ of the spin-polarized regions diverges at the Stoner transition, where κ is the inverse decay length. In the case of Co₂Si nanoclusters, this mechanism leads to strongly spinpolarized surface atoms (shell) with relatively weak magnetic interior atoms (core) and subsequently makes the clusters ferromagnetic [22]. Finally, the inversion-symmetric crystal structure of Co_2Si is orthorhombic (point group D_{2h} , space group *Pmna*) [25], so that two anisotropy constant K_1 and K'_1 are necessary for the description of the magnetocrystalline anisotropy.

^{*}bbalasubramanian2@unl.edu

[†]dsellmyer@unl.edu

This study presents the magnetic and electron-transport properties of Co₂Si nanocluster films, where we expect interesting temperature-dependent effects. Since orthorhombic crystals tend to have substantial magnetocrystalline anisotropies, thermally activated magnetization changes involving whole clusters is not very likely to occur at room temperature. They are much easier to realize in shells, where much smaller switching volumes can be realized. In this paper, Sec. II is devoted to a basic analysis of magnetization effects in weakly ferromagnetic nanostructures, and Sec. III describes the sample preparation and measurement methods. In Sec. IV, we present the experimental results and analyze the magnetotransport behavior in terms of the orthorhombic anisotropy.

II. THEORETICAL BACKGROUND ON WEAK FERROMAGNETISM

The focus of this section is on how thermal effects, field-induced changes of the magnetic moment, and micromagnetic contributions affect the field-dependent magnetization, M(H) curves. If the clusters were made from strong ferromagnetic elemental Co, then the high-field contributions due to spin rotation and moment change yield only a small high-field susceptibility χ_0 and can be separated easily from the micromagnetic contributions. In materials close to the Stoner criterion, such as Co_2Si , different contributions are more convoluted and a great care is necessary in the interpretation of M(H).

Strongly exchange-enhanced Pauli paramagnets and very weak itinerant ferromagnets (VWIFs) are close to but on different sides of the Stoner criterion $I(E_{\rm F})=1$. To streamline the notation, we will refer to these two limits as Bloch magnetism, because the wave functions are almost Bloch like. The free energy per unit volume of an isotropic Bloch magnet is given by the Landau expansion [24,26]

$$F = \frac{1}{2}aM^2 + \frac{1}{4}bM^4 + c(\nabla M)^2 + E_a(M) - \mu_o \mu_B HM, \quad (1)$$

where M is the local magnetization measured in μ_B per atom, E_a is the anisotropy energy, and a, b, and c are phenomenological coefficients. The free energy in Eq. (1) leads to a complicated nonlinear differential equation without a known solution. However, the a and b terms normally dominate the anisotropy energy, so that we will ignore E_a in this section and treat it perturbatively in Sec. IV A. The coefficient, exchange-enhanced Pauli susceptibility, $\chi \sim 1/\kappa^2$, which has been dealt with in Ref. [22], yields a zero-field magnetization M that is aligned in relatively small fields and enhances M = |M| in strong fields. However, an applied field also spin polarizes the interior of the cluster, and to determine this effect, we need to estimate a and b.

Paramagnetic and ferromagnetic phases have a>0 and a<0 respectively, so one can write that $a\sim T_{\rm c}-T$, which was Landau's original reasoning. The zero-temperature limit is fairly well described by $a=1/\mathcal{D}-I$ and $b=1/\mathcal{D}$ [27], where \mathcal{D} is density of states. Near the Stoner transition, the Landau and zero-temperature terms can be added in a rough quantum-mechanical approximation [28] and one obtains

$$a = k_{\rm B}T + 1/\mathcal{D} - I. \tag{2}$$

Since a = 0 at the Curie point, this equation yields $T_c = (I - 1/D)$ for VWIFs. By keeping the a and H terms only in Eq. (1) and then minimizing F, one can show that Eq. (2) reproduces a Curie-Weiss law with $\theta = I - 1/D$ for perfectly homogeneous Bloch magnets.

It is important to note that the predictions from Eqs. (1) and (2) differ from predictions based on the Brillouin function. In the high-field limit, Eq. (2) yields saturation in fields of the order of $\mu_0\mu_B\mathcal{D}$ (several 100 T), whereas the Brillouin function predicts a much more rapid saturation at low temperatures. The reason is that the latter describes spin *rotations* under the competing influences of thermal disorder (at most several 100 K) and Zeeman interaction. In the Bloch limit, the field changes the *magnitude* of the spin moment per atom and competes against electron energies of the order of $1/\mathcal{D}$ (about 10 000 K in temperature units).

Applied to Co_2Si nanoclusters, Eq. (1) yields the following scenario. Surfaces spin polarize the interior of the clusters as observed in Ref. [22], but the random crystalline orientation of the clusters, described by the anisotropy term, means that some field is necessary to align the magnetization. On top of this micromagnetic magnetization change, commonly known as the "approach to saturation," there is also an influence from the temperature-dependent susceptibilities of surface atoms and of the adjacent interior atoms, the former being of a Brillouin type and the latter being of the Bloch type. Finally, very high fields create a Bloch-type magnetic moment everywhere in the clusters.

In a diamagnet or ordinary Pauli paramagnet, the high-field magnetization change is a very small correction, which can be described by a magnetization contribution $\chi_0 H$. In the present system, the centers of the particles are in the Bloch regime and therefore yield a fairly strong nonlinear contribution to M(H). In terms of Eq. (1), we ignore the gradient and anisotropy terms, which are very small in the interior of the particles. Minimizing F with respect to M then yields the cubic equation

$$\mu_o \mu_B H = aM + bM^3. \tag{3}$$

This equation is equivalent to Eq. (9) in Wohlfarth's analysis [29]. For example, putting H = 0 yield the spontaneous magnetization $M_s = \sqrt{|a|/b}$ for a < 0 and $M_s = 0$ for a > 0.

Equation (3) is also well known in statistical mechanics [26], where it yields the respective mean-field critical exponents $\gamma=1$ and $\delta=1/3$ for the susceptibility dM/dH and the critical isotherm M(H), both valid near the critical point $T=T_{\rm c}$ (or a=0), H=0, and M=0. Our case is different, because a is small but nonzero, whereas both H and M are fairly high. We can, however, solve Eq. (3) by series expansion, starting from high values of H and treating H as a small correction. The lowest-order term is independent of H and yields, in the units of Eq. (1),

$$M = (\mu_{\rm o}\mu_{\rm B}H/b)^{1/3} \sim H^{1/3}.$$
 (4)

Unlike the formally identical critical isotherm, the equation cannot be used for very small fields. Note that the $H^{1/3}$ term is clearly identifiable in high-field experiments [29,30]. At very high fields (several 100 T), the applicability of Eq. (1) breaks down, but in the intermediate field range of interest in the present context, it is quite accurate. A key feature of Eq. (4) is that M(H) has a negative curvature d^2M/dH^2 ,

compared to the zero curvature of $M = \chi_0 H$. As we will discuss in Sec. IV A, this curvature is visible in careful fitting and allows us to separate the "approach to saturation" contribution proportional to $-1/H^2$, which also has a negative curvature.

III. SAMPLE PREPARATION AND EXPERIMENTAL METHODS

The Co₂Si nanoclusters were fabricated using an inert-gas condensation-type cluster-deposition method [22]. In brief, the Co₂Si nanoclusters were produced in a cluster-formation chamber by sputtering a Co-Si composite target using a mixture of argon (Ar) and helium (He) gases and extracted as a collimated beam towards a deposition chamber, where they are deposited on substrates kept at room temperature. A schematic of the cluster-deposition process is also shown in Supplemental Material S1 [31]. The substrates are singlecrystalline Si (001) with a 100-nm-thick thermal oxide. The cluster size can be generally controlled by adjusting dc magnetron sputtering power and gas flow rates. In the case of Co₂Si nanocluster samples, the Ar flow rates were mostly varied from 200 to 750 SCCM (standard cubic centimeter per min) to decrease the average cluster size [22]. The Co₂Si nanoclusters investigated in this study were prepared using a dc magnetron sputtering power of 200 W, while maintaining the flow rates of Ar and He as 400 and 100 SCCM, respectively. The base pressure in the cluster-formation chamber is about 1×10^{-7} Torr. First, this chamber was purged with Ar and He and subsequently evacuated to the base pressure $(1 \times 10^{-7} \, \text{Torr})$ for several times and then kept at a continuous flow of Ar and He at the working pressure of about 0.8 Torr for about 2 h prior to sputtering, in order to have oxygen free growth environment.

The nanoclusters were deposited for an extended time to form dense films on Au electrode-coated substrates for electron-transport measurements. For magnetic measurements, the nanocluster films were deposited on bare Si substrates. Compared to wet-chemical methods, the clusterdeposition method has an advantage that nanoclusters can be deposited as dense films directly on any substrates and electrodes without affecting the size, shape, and structure of the clusters. Nanocluster films produced by cluster deposition are isotropic irrespective of their shapes, because their crystallographic axes are randomly oriented [16,22]. The present nanoclusters are also isotropic, as evidenced by the relative intensities of the Rietveld-analyzed x-ray diffraction peaks (Supplemental Material S2 [31]). In fact, anisotropic (textured) ensembles are highly desired in permanent magnetism but nontrivial to achieve, for example, by applying a magnetic field prior to deposition [16,22].

Figure 1 illustrates the steps involved in the fabrication of the sample for transport measurements. First, a 5-nm-thick titanium (Ti) film was deposited on Si substrate, followed by the deposition of a 25-nm-thick gold (Au) film using a dc magnetron sputtering through mask A [Fig. 1(a)]. Second, mask A was removed, and the substrate was aligned with mask B and loaded in the cluster-deposition system. A $\rm Co_2Si$ nanocluster film of about 270 nm thickness, 5 mm length, and 0.5 mm width was then deposited through mask B using the cluster-deposition process, and this step was immediately

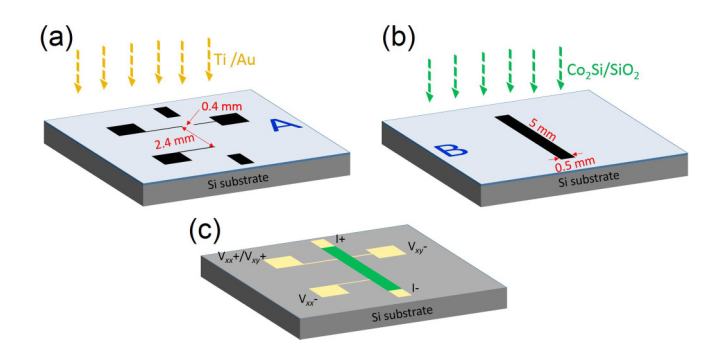


FIG. 1. Schematics of sample fabrication steps for electron-transport measurements using bar-shaped shadow masks: (a) Deposition of a 5-nm-thick Ti film on a single-crystalline Si (001) substrate followed by a 25-nm-thick Au film through mask A. (b) A 270-nm-thick Co_2Si nanocluster film followed by a 10-nm-thick SiO_2 cap layer deposition through mask B. (c) Final device structure.

followed by the deposition of a 10-nm-thick SiO_2 cap layer using a radio-frequency sputtering gun employed in the deposition chamber [Fig. 1(b)]. The purpose of the cap layer is to prevent possible oxidation upon exposure to air. Removal of mask B yields the final device structure for the transport measurements, as schematically shown in Fig. 1(c).

Longitudinal resistivity (ρ_{xx}), magnetoresistance (MR), and Hall resistivity data (ρ_{xy}) were measured as a function of temperature and magnetic field using a Quantum Design Physical Property Measurement System (PPMS). Magnetic properties were measured using a Quantum Design MPMS superconducting quantum-interference device (SQUID). X-ray diffraction and transmission-electron microscopy show that Co₂Si nanoclusters form an orthorhombic structure of prototype Co₂Si and space group *Pnma* (Supplemental Material S2 [31]). The Co₂Si nanoclusters investigated in this study have an average size $d \approx 11.3$ nm with a standard deviation of $\sigma/d \approx 0.19$ as shown in Supplemental Material S2 [31].

IV. RESULTS AND DISCUSSION

This paper mainly deals with the nanoscale magnetic structure of the ensemble of clusters as schematically shown in Fig. 2, and how this structure affects the electron-transport properties of the system. In this section, we first consider the magnetic properties, and then discuss the magnetotransport

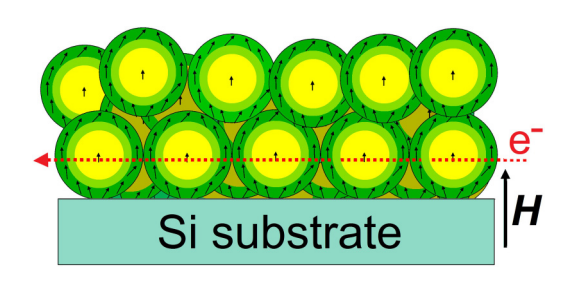


FIG. 2. Co_2Si nanoclusters: Schematic of a deposited thin film. The magnetization (arrows) is largely confined to a surface layer (green). The simplest conduction path through contacts is indicated by the red-dotted line.

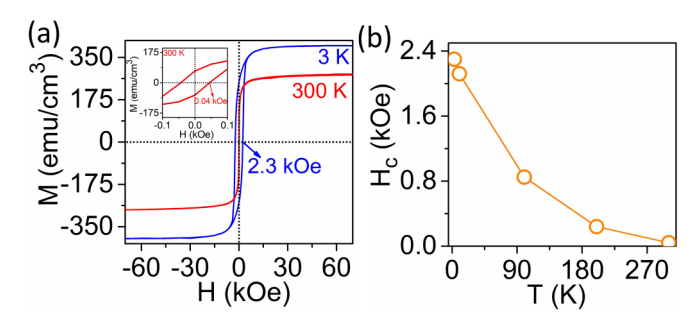


FIG. 3. Magnetic properties: (a) Field-dependent magnetization curves measured at 300 and 3 K, where the inset shows the expanded room-temperature hysteresis loop in the low-field region and (b) coercivity H_c as a function of temperature.

properties, which are strongly dependent on the magnetic properties.

As discussed in Secs. I and II and illustrated in Fig. 2, the local moments of Co₂Si clusters are situated predominantly at the surfaces, and those moments spin polarize the interior atoms leading to ferromagnetism, albeit of an inhomogeneous type. The radial distribution of magnetic moments in the Co₂Si clusters strongly depends on the inverse decay length κ [22]. There is no systematic dependence of κ on the cluster size, although the experimental value of 1.3/nm for relatively big clusters is somewhat smaller than the DFT prediction of 2.3/nm, obtained for very small clusters [22]. Since κ strongly depends on the local Co concentration, inaccuracies in the composition in the core as well as concentration gradients near the surface may explain the difference. On the other hand, the temperature dependence of the shell thickness is approximately given by Eq. (2), via $\kappa \sim \sqrt{a}$. Assuming that the core is "nonmagnetic" (a strongly exchange-enhanced Pauli paramagnet), κ and the decay length $1/\kappa$ increase and decrease with increasing temperature, respectively.

A. Magnetic properties

The field-dependent magnetization measured at 3 and 300 K for Co_2Si nanoclusters deposited, Fig. 3(a), is characteristic of ferromagnetic hysteresis. The Si substrate only exhibits a very weak diamagnetic background, which was subtracted from the raw data (Supplemental Material S3 [31]). The temperature dependence of coercivity H_c is plotted in Fig. 3(b). The relatively high coercivity of $H_c = 2.3$ kOe at 3 K, compared to 0.04 kOe at 300 K, reveals significant low-temperature magnetocrystalline anisotropy associated with the noncubic orthorhombic structure.

In Fig. 4(a), we analyze the field dependence of the magnetization in terms of the approach-to-saturation expression [32–34]

$$M = M_s \left(1 - \frac{4K_{\text{eff}}^2}{15M_s^2 H^2} \right) + \chi_o H + pH^{1/3},$$
 (5)

where $K_{\rm eff}$ and $M_{\rm s}$ are the effective magnetic anisotropy constant and saturation magnetization, respectively. Note that the $H^{1/3}$ asymptotic discussed in Sec. II affects the approach to saturation, and in order to take this effect into account, the term $pH^{1/3}$ corresponding to the VWIF of the cluster core is

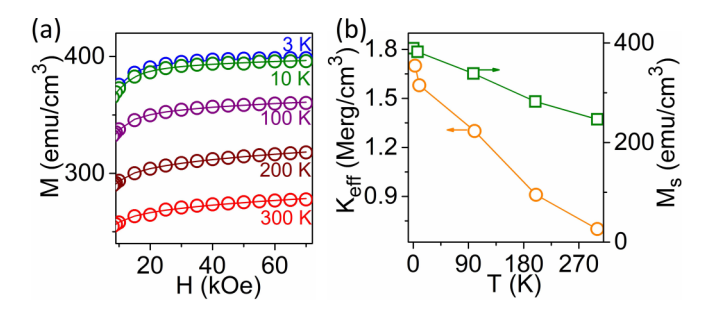


FIG. 4. Approach-to-saturation analysis: (a) Fitting of the field-dependent magnetization data using Eq. (5) at different temperatures. The open circles and solid lines correspond to the experimental data and fittings, respectively. (b) Effective anisotropy constant $K_{\rm eff}$ and saturation magnetization $M_{\rm s}$ as a function of temperature.

added to the original approach-to-saturation expression discussed in Refs. [32,33]. Without the $pH^{1/3}$ term, the Eq. (3) underestimates the M(H) curvature. As one can see from Sec. II, the parameter p reflects the competition between Zeeman (\sim 0.1 eV) and electronic interactions ($I \approx 1/\mathcal{D} \sim 1$ eV). It depends on the details of the electronic structure (density of states) but is of the order of $\alpha^{2/3}M_{\rm s}=0.0376M_{\rm s}$, where $\alpha=1/137$ is Somerfield's fine-structure constant.

Figure 4(a) shows the fitting of experimental magnetization data in the approach to saturation region (H = 10 to 70 kOe) using Eq. (5), where M_s , $K_{\rm eff}$, and p have been used as fitting parameters. Note that the $\chi_0 H$ contribution is negligibly small in low fields and at low temperatures [33,35]. Furthermore, in the present system, p also actually involves χ_0 , reproducing the latter in the limit of strong ferromagnetism at high-field region. Therefore $\chi_0 H$ term is not separately required and excluded during the fitting. At 300 K, the experimental value of p is $0.06M_s$ and the fitting also yields $K_{\text{eff}} = 0.7 \,\text{Merg/cm}^3$ and $M_s = 248 \,\mathrm{emu/cm^3}$. K_{eff} and M_s obtained using this analysis at different temperatures are shown in Fig. 4(b). As in other systems with lowest-order (second-order) magnetic anisotropy [36], the magnetocrystalline anisotropy shows a moderate decrease with increasing temperature. Note that the application of the uniaxial expression Eq. (5) to orthorhombic crystals is nontrivial and requires explicit justification (see below).

Equation (5) indicates that the magnetization changes involve both zero-temperature and temperature-dependent contributions. Figure 4(a) and the corresponding approach to saturation analysis shows that χ_0 is indeed almost constant at each temperature. This makes it possible to separate high-and low-field contributions and to analyze the anisotropy energy $E_a(M)$ in Eq. (1) with the help of the approach to saturation, Eq. (5). However, Eq. (5) is based on the uniaxial energy expression $E_a(M) = K_{\rm eff} V_{\rm uc} \sin^2 \theta$, where $K_{\rm eff} = K_1$ is the first anisotropy constant and $V_{\rm uc}$ is the unit-cell volume. Orthorhombic crystals are nonuniaxial and, in lowest order [36], described by

$$\frac{E}{V_{uc}} = K_0 + K_1 \sin^2\theta + K_1^{'} \sin^2\theta \cos 2\varphi. \tag{6}$$

 K_1 and K'_1 as well as the physically unimportant zero-point energy constant K_0 can be determined using

density-functional theory (DFT) by calculating the total energy per unit cell (u.c.) for different magnetization directions or angles θ and ϕ [37,38]. The calculated values of K_1 and K_1' for a Co_2Si cluster containing 96 atoms are $-3.89\,\mathrm{Merg/cm^3}$ ($-0.389\,\mathrm{MJ/m^3}$) and $K_1'=-0.66\,\mathrm{Merg/cm^3}$ ($-0.066\,\mathrm{MJ/m^3}$), respectively (Supplemental Material S4 [31]). The negative values of K_1 and K_1' indicate that Co_2Si has basically easy-plane anisotropy, accompanied by a substantial anisotropy in the basal plane.

As mentioned above, Eq. (5) was originally derived for uniaxial crystals with easy-axis anisotropy $(K_1 > 0)$. Its applicability to easy-plane magnets $(K_1 < 0)$ is somewhat counterintuitive, because one may expect the free magnetization rotation in easy-plane magnets to yield a faster approach to saturation. In fact, this is not the case, and Eq. (5) can equally be used for easy-plane magnets. Formally, changing the K_{eff} in Eq. (5) from $+K_1$ to $-K_1$ does not affect M(H).

Orthorhombic anisotropy is a different scenario, because K_{eff} is likely to involve both K_1 and K'_1 . Since the Co₂Si clusters are not aligned crystallographically, the a, b, and c vectors point in random directions, constrained by the requirement that they can be orthogonal to each other. To obtain M(H), one must perform an average over all crystallite directions, and the underlying mathematical problem was solved by Danan and Barbier [34]. From Ref. [34], we obtain

$$K_{\rm eff} = \sqrt{K_1^2 + 3 K_1^{'2}}.$$
 (7)

This equation shows that the basal-plane anisotropy K'_1 yields a disproportionally large contribution to the effective anisotropy, in spite of often being smaller than K_1 . We also see that the signs of K_1 and K'_1 do not matter in the asymptotic approach to saturation.

Using the K_1 and K_1' values from the DFT calculations, we obtain $K_{\rm eff} = 4.0 \, {\rm Merg/cm^3}$, which is in fair agreement with the experimental value of $K_{\rm eff} = 1.7 \, {\rm Merg/cm^3}$ at 3 K. The difference is not surprising, because the experimental clusters (11.3 nm size) are bigger than the DFT clusters (1.3 nm) and the magnetocrystalline anisotropy of nanoclusters tends to increase with decreasing size [39,40]. One aspect of this dependence is the surface-to-volume ratio but other, more difficult to quantify factors such as surface plane indices also matter [41].

Note that magnetic anisotropy is a key intrinsic property to develop thermal stability in nanomagnets. It is also worthwhile to note that the thermal demagnetization only affects isolated or very weakly interacting clusters and the blocking temperature of *isolated* magnetic nanoclusters is proportional to $K_{\rm eff}V$, which describes the whole cluster. However, as explained in the experimental section and illustrated in Fig. 2, our nanoclusters are formed as a densely packed thin film, so that the exchange coupling between the clusters suppresses the superparamagnetic fluctuations. This finding is confirmed by the observation of a nonzero room-temperature coercivity of about 0.04 kOe [see inset of Fig. 3(a)].

Magnetic interactions are indeed important, because the clusters touch each other. This contact makes the system conductive (Sec. IV B)—isolated clusters would have an infinite resistivity, and the corresponding intercluster exchange interaction suppresses superparamagnetism. Note that the

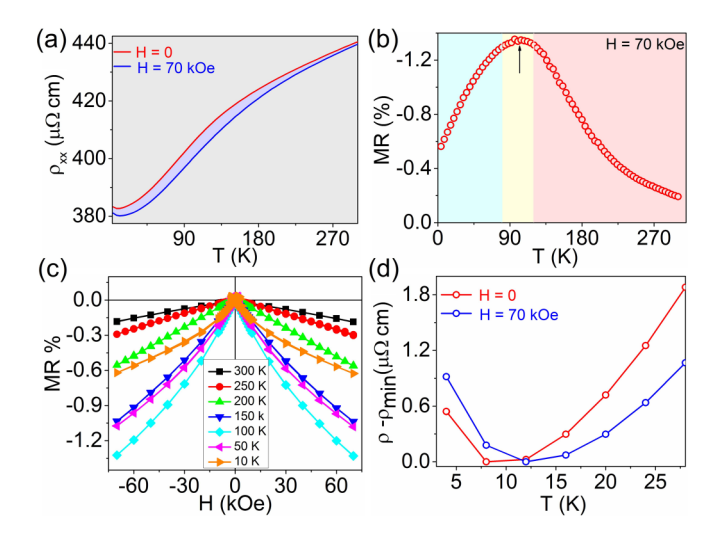


FIG. 5. Magnetotransport measurements: (a) Longitudinal resistivity ρ_{xx} measured in magnetic fields of 0 and 70 kOe. (b) Temperature-dependent magnetoresistance (MR) in a field of 70 kOe. (c) Field dependence of magnetoresistance measured at different temperatures. (d) The $\rho_{xx}(T)$ in (a) is subtracted from the minimum value to visualize clearly T_{\min} at which the resistivity starts to increase on decreasing temperature.

primary focus of Eq. (1) is on the local magnetic moment, but this equation can also be used to discuss intercluster interactions, in analogy to Ref. [41]. Figure 16 and Eq. (4.26) in Ref. [41] show that the interparticle exchange is surprisingly strong even if the exchange is strongly reduced in the contact region between grains or clusters. Similarly, the change in the magnitude of the spin moment per atom is a well-established fact in very weak itinerant ferromagnets and strongly exchange-enhanced Pauli paramagnets [23,27,29]. This change is unrelated to micromagnetic phenomena such as superparamagnetic blocking and coercivity, and Eq. (1) describes how it is realized in ensembles of isolated or compressed nanoparticles.

B. Electron-transport properties

The temperature dependence of the resistivity ρ_{xx} of the Co2Si nanocluster film has been measured in 0- and 70-kOe magnetic field. The data, shown in Fig. 5(a), reveal the metallic nature of the sample, but the resistivity of the nanocluster film, for example at room temperature (440 $\mu\Omega$ cm), is higher than that of nanobelts (213 $\mu\Omega$ cm), bulk crystal $(190 \,\mu\Omega \,\mathrm{cm})$, and nano wires $(200 \,\mu\Omega \,\mathrm{cm})$ [42]. This is not surprising, because the conduction is realized through the contact points between the nanoclusters. The change in the slopes of the curves in Fig. 5(a) around 150 K may be an electronic effect associated with the peaked density of states near the Fermi level [22]. In contrast to strong ferromagnets (such as Co) and ordinary weak ferromagnets (such as Fe), the low-temperature behavior of very weak itinerant ferromagnets (and of strongly exchanged enhanced Pauli paramagnets) is largely determined by the density of states (DOS) at the Fermi level. At elevated temperatures, the behavior of these Blochtype magnets becomes more and more reminiscent of strong ferromagnets [28,43]. The local DOS at the surface [Fig. 3(a) in Ref. [22]] indicates strong ferromagnetism (complete 3 d spin polarization), whereas the core is of the Bloch type [Fig. 3(b) in Ref. [22]]. Therefore, the DOS is very high, close to the Stoner transition. Furthermore, the peaks in the DOS are very narrow (about 50 meV), so that major electron-redistribution effects occur at rather low temperatures and possibly results in the slope change around 150 K in Fig. 5(a).

Figure 5(b) shows that the magnetoresistance (MR%), defined as $\{[\rho_{xx}(H) - \rho_{xx}(0)]/\rho_{xx}(0)\} \times 100$, is negative throughout the temperature range. Negative MR is a general feature of ferromagnetic metals, because spin misalignment yields scattering. The applied magnetic field suppresses spatial fluctuations of the spin direction and thereby reduces the resistance [44]. As a function of temperature, the MR shows a nonmonotonic change of magnetoresistance and its magnitude exhibits a maximum near 100 K, Fig. 5(b). The same behavior is also seen in the field-dependent MR data measured at different temperatures, Fig. 5(c). There is also a small resistivity upturn below 15 K, as shown in Figs. 5(a) and 5(d). The resistance minimum is often observed in some strong ferromagnets due to Kondo effect [45-47]. The original Kondo effect involves interactions between localized and delocalized electrons, but a minimum can also be caused by Mott-Hubbard and (one-electron) Anderson localizations [48,49].

The magnetoresistance of the films is dominated by the local nanoscale magnetic structures near the contacts between the clusters. The electron scattering increases with the magnetization gradient, which is controlled by Erdmann-Weierstrass (EW) boundary conditions [41,50–52] and is particularly large near interfaces (see, e.g., Sec. 4.5 in Ref. [41]). A specific feature of our Co₂Si system is the involvement of the spin-polarized shell. At low temperatures, the mean-free path of the electrons is much larger than the cluster diameter, whereas at room temperature, both lengths are comparable. This leads to two main types of scattering events. The first mechanism consists in the reflection of electrons at the inner surfaces while the electrons stay inside the cluster. This scattering occurs in random directions, acts as a type of surface-scattering mechanism, and thus decreases the conductivity. The second mechanism, schematically illustrated in Fig. 6, shows how electrons move through contact points and are therefore responsible for the conduction. The MR reflects the spin structure near the contact points: the resistance in Fig. 6(a) is higher than that in Fig. 6(b), because the spins are less aligned in 6(a). The spin structure, as affected by thermal disorder and magnetocrystalline anisotropy, is explained below.

The magnetoresistance data, Figs. 5(b) and 5(c), show an interesting temperature-dependent nonmonotonic behavior with a maximum magnitude at about 100 K. To understand the maximum in MR, we must analyze the spin structure of Fig. 6 as a function of the magnetic field. We have shown that the high-field magnetization of the nanoclusters is roughly proportional to $H^{1/3}$ whereas the slope χ_0 is almost constant for small-to-medium fields. The magnetoresistance maximum in Fig. 5(b) reflects the magnetocrystalline anisotropy, which favors magnetization orientation along the randomly oriented local [100] or a axis. The anisotropy competes against the ferromagnetic interatomic exchange and the external magnetic

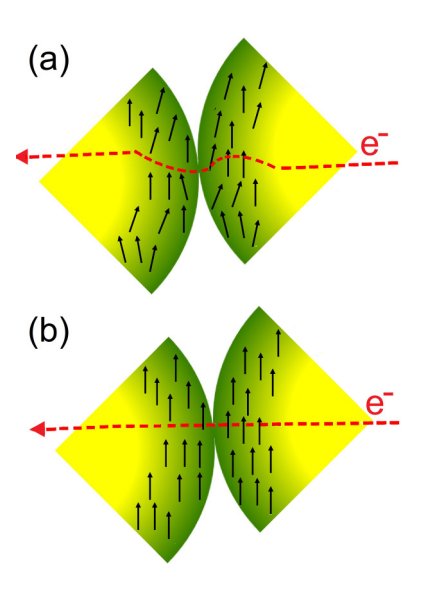


FIG. 6. Magnetoresistance in compacted Co_2Si nanoclusters (schematic): (a) Relatively high resistance due to spin misalignment ($\nabla M \neq 0$). (b) Relatively low resistance due to spin alignment in a magnetic field or by interatomic exchange ($\nabla M = 0$). There are many electron trajectories, but only the ones that go through the contact points contribute to the conduction (dashed red lines).

field, which both favor parallel spin alignment. The anisotropy is highest at low temperatures, where it leads to a freezing of the misaligned spins. On increasing temperature, magnetic anisotropy decreases and at about 100 K, both the anisotropy and the coercivity are strongly reduced, Figs. 3(b) and 4(b). This means that the local magnetization is easily aligned by the external magnetic field, leading to an increase in magnetoresistance. Above about 100 K, the anisotropy further decreases and is no longer able to effectively compete. On the other hand, the mean free path becomes comparable to or smaller than the cluster size at room temperature. Therefore, the scattering contribution becomes more dominant on increasing temperature towards 300 K and this leads to a decrease in the magnetoresistance.

We also have investigated the anomalous Hall effect in the Co₂Si nanocluster film. In general, there are surprisingly only a few reports on the AHE of nanoclusters or particles [6]. This is possibly due to the difficulties in sample preparation using nanoparticles for Hall measurements. As discussed in Sec. III, the cluster-deposition method uniquely makes it possible to deposit a dense film of nanoclusters on a Hall bar. The fielddependent Hall resistivity data ρ_{xy} measured at 10 K is shown in Fig. 7(a) (black curve). The Hall resistivity, $\rho_{xy} = R_0 B +$ $4\pi MR_s$, is composed of an ordinary term $\rho_{OH} = R_0 B$ and an anomalous term $\rho_{AH} = 4\pi M R_s$. R_0 and R_s are the ordinary and anomalous Hall coefficients, respectively. $B = B_0 + 4\pi M$ (1 - N) is the flux density or magnetic-field induction, where $B_0 = H$ in G (cgs) or $\mu_0 H$ in T (SI) is the applied (external) magnetic field. Note that the demagnetization factor N = 1for thin films in a perpendicular magnetic field [1,53-55], and therefore the Hall resistivity for Co₂Si nanocluster film is considered as $\rho_{xy} = R_0 H + 4\pi M R_s$ or $R_0 B_0 + 4\pi M R_s$.

Note that the magnetization data of the Co_2Si nanocluster film [Fig. 4(a)] clearly show the approach to saturation

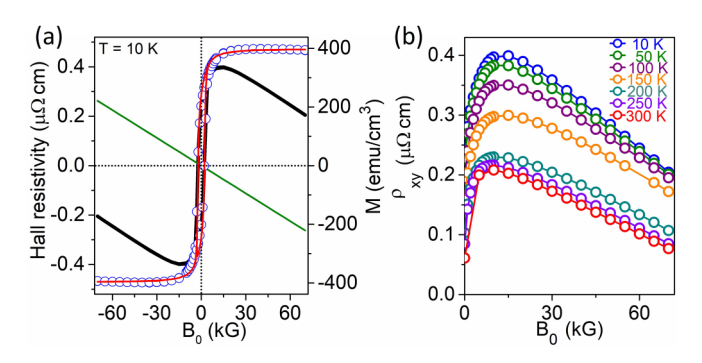


FIG. 7. Temperature and field dependence of the Hall effect: (a) Anomalous Hall effect at 10 K as a function of external magnetic field [$B_0 = H$ in G (cgs) or $\mu_0 H$ in T (SI)]. The figure shows the field dependence of the Hall resistivity (black curve), ordinary Hall effect (green line), and AHE contribution (open circle) in $\mu\Omega$ cm. Field-dependent magnetization data in emu/cm³ is also given for comparison (red curve). (b) Field-dependent ρ_{xy} measured at different temperatures.

above $B_0 = 20 \,\mathrm{kG}$ ($H = 20 \,\mathrm{kOe}$), and this leads to the anomalous term as constant $(4\pi M_s R_s)$ in the high-field region. Therefore, the linear fitting to the ρ_{xy} data in the high-field region (20-70 kOe), shown in Supplemental Material S5, yields R_0 (slope) and $\rho_{AHE} = 4\pi M_s R_s$ (intercept to the y axis) [31,56,57]. R_0 and R_s are subsequently obtained using this analysis at 10 K as -0.37×10^{-5} and $9.37 \times 10^{-5} \mu\Omega$ cm/G, respectively. The sign of R_0 often reflects the type of the charge careers [53,58], and is negative in this study, which indicates predominantly electronlike conduction in Co₂Si nanoclusters. Note that R_0 and R_s have often the same sign, but there are exceptions [58,59]. One example is $Ni_{1-x}Pt_x$ films [58], a system close to the onset of ferromagnetism and therefore reminiscent of Co₂Si. The sign of the anomalous Hall effect also depends on the spin direction of the carriers and cannot be simply related to electron- and hole-type contributions. By subtracting the ordinary Hall-effect contribution, the Hall resistivity due to the anomalous Hall effect (AHE) is obtained [open circle in Fig. 7(a)], whose shape is similar to the M(H) data obtained at 10 K (red curve).

Figure 7(b) shows the field-dependent ρ_{xy} data measured at different temperatures for the Co₂Si nanocluster film. The linear fitting to the ρ_{xy} data in the high-field region at different temperatures (Supplemental Material S5 [31]) are also carried out to obtain the temperature-dependent R_0 and ρ_{AHE} . The ordinary Hall coefficient (R_0) and the effective carrier concentration determined using the relation $R_0 = -1/ne$ (e is the electronic charge) are plotted as a function of temperature as shown in Fig. 8. Note that the subtle changes in the density of states are indeed reflected in the temperature-dependent evolution of the ordinary Hall effect. The ordinary Hall coefficient (R_0) and the effective carrier concentration (n) show a significant temperature-dependent change for $T \leq 150 \,\mathrm{K}$ as shown in Fig. 8. This result is consistent with the interpretation of the slope change of the resistivity curves around 150 K in Fig. 5(a) being an electronic effect.

The ρ_{AHE} values are plotted as a function of temperature as shown in Fig. 9(a). Normally, ρ_{AHE} in ferromagnetic metals increases with temperature [1,60,61] but Co₂Si

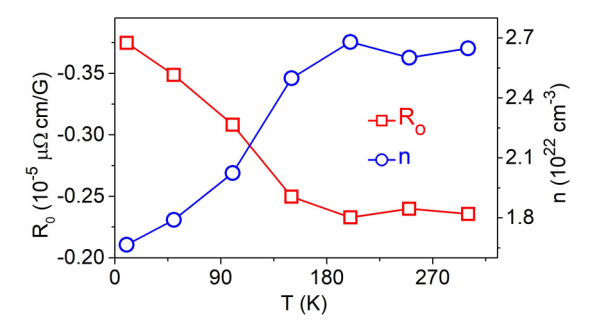


FIG. 8. Temperature dependence of ordinary Hall contribution: ordinary Hall coefficient R_0 and effective carrier concentration n.

nanoclusters show an opposite trend. First, R_s often depends on ρ_{xx} , $R_s = a_{xx} + b_{xx}^2$ [1,62], and ρ_{xx} exhibits only some weak temperature dependence, Fig. 5(a). However, the saturation magnetization decreases significantly by about 36.2%, from 390 to 248 emu/cm³, when going from 3 to 300 K, Fig. 4(b). Therefore it is likely that the temperature-dependent decrease of magnetization is the cause for the decrease in $\rho_{AHE} = 4\pi M_s R_s$ on increasing temperature.

The Hall conductivity σ_{AHE} is often scaled with the longitudinal conductivity σ_{xx} to understand the anomalous Hall effect [1,63]. The Hall conductivities at different temperatures were determined using the corresponding ρ_{AHE} and ρ_{xx} values [64–67] and plotted as a function of σ_{xx} as shown in Fig. 9(b) (open black circles). As mentioned above, the change of Hall resistivity at different temperatures are mainly caused by the temperature-dependent saturation magnetization and therefore it is also worthwhile to see how the Hall conductivity at constant magnetization varies with σ_{xx} . For this, we have normalized σ_{AHE} by $M_s(T)/M_s$ (10 K), and the normalized Hall conductivity σ'_{AHE} (red triangles) is also shown in Fig. 9(b).

The σ_{AHE} and σ'_{AHE} increase with σ_{xx} as shown in Fig. 9(b). σ_{xx} and σ_{AHE} of the nanocluster film varies between $2.27 \times 10^3 - 2.61 \times 10^3$ and $1.25 - 3.21 \, \Omega^{-1} \, \mathrm{cm}^{-1}$, respectively. It is worthwhile to note that Onoda *et al.* have summarized magnetic materials having different ranges of longitudinal and Hall resistivities (Fig. 12 in Ref. [63]). Several

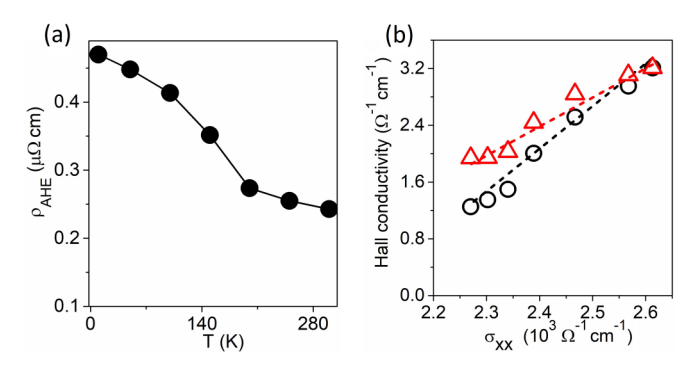


FIG. 9. Anomalous Hall contributions: (a) Anomalous Hall resistivity $\rho_{\text{AHE}} = 4\pi R_s M_s$ as a function of temperature. (b) Dependence of anomalous Hall conductivities σ_{AHE} (open black circles) and σ'_{AHE} (open red triangles) as a function of longitudinal conductivity σ_{xx} . The black- and red-dashed lines are linear fits to the corresponding data and shown for guide to eye.

materials having σ_{xx} in the range $10^3-10^4~\Omega^{-1}~cm^{-1}$ have shown Hall conductivities similar to Co_2Si nanocluster films and a few systems are briefly mentioned below. For example, $Cu_{1-x}Zn_xCr_2Se_4$ alloys with $\sigma_{xx}\approx 10^3~\Omega^{-1}~cm^{-1}$ exhibit Hall conductivity of about $10~\Omega^{-1}~cm^{-1}$ [63,68]. Similarly, FePt films with a thickness of 1.3 nm and $\sigma_{xx}\approx 10^3~\Omega^{-1}~cm^{-1}$ have shown $\sigma_{AHE}\approx 2~\Omega^{-1}~cm^{-1}$ [48]. Note that it is challenging to establish a meaningful power-law dependence and scattering mechanism due to the narrow conductivity range of the nanocluster samples. However, the conductivity of our system is close to the region where the intrinsic mechanism becomes dominant [1,63].

V. CONCLUSIONS

We have investigated the temperature-dependent magnetic and spin-electronic properties of Co₂Si nanocluster films. Our ensembles of nanoclusters exhibit several intriguing features associated with the electronic structure of Co₂Si. The magnetotransport in the films is characterized by a cluster size smaller than or comparable to the mean free path, an

electronic structure close to the Stoner criterion, and orthorhombic anisotropy. The anisotropy, which is analyzed in terms of a modified law of approach to saturation, yields an unusual temperature dependence of the magnetoresistance. The present paper is a prime example on how nanostructuring creates a new material with unique combination of electronic, magnetic, and transport properties.

ACKNOWLEDGMENTS

This research was primarily supported by the U.S. Department of Energy under Award No. DE-FG02-04ER46152 and the National Science Foundation—Designing Materials to Revolutionize and Engineer our Future: Sustainable Chemistry, Engineering, and Materials (NSF-DMREF: SusChEM), under Grant No. 1729288. This work was performed in part in the Nebraska Nanoscale Facility, Nebraska Center for Materials and Nanoscience, which is supported by the National Science Foundation under Award No. ECCS: 2025298, and the Nebraska Research Initiative (NRI). We thank S. R. Valloppilly for helpful discussions.

- [1] N. Nagaosa, J. Sinova, S. Onoda, A. H. MacDonald, and N. P. Ong, Rev. Mod. Phys. 82, 1539 (2010).
- [2] L. Zhou, H. Song, K. Liu, Z. Luan, P. Wang, L. Sun, S. Jiang, H. Xiang, Y. Chen, J. Du, H. Ding, K. Xia, J. Xiao, and D. Wu, Sci. Adv. 4, eaao3318 (2018).
- [3] H. Wang, C. Lu, J. Chen, Y. Liu, S. L. Yuan, S.-W. Cheong, S. Dong, and J.-M. Liu, Nat. Commun. 10, 2280 (2019).
- [4] T. Seki, S. Iihama, T. Taniguchi, and K. Takanashi, Phys. Rev. B 100, 144427 (2019).
- [5] N. J. Ghimire, A. S. Botana, J. S. Jiang, J. Zhang, Y.-S. Chen, and J. F. Mitchell, Nat. Commun. 9, 3280 (2018).
- [6] G. Song, M. Ranjbar, D. R. Daughton, and R. A. Kiehl, Nano Lett. 19, 7112 (2019).
- [7] T. J. Pearson and D. E. Freedman, ACS Cent. Sci. 4, 1092 (2018).
- [8] B. H. Zhou and J. D. Rinehart, ACS Cent. Sci. 4, 1222 (2018).
- [9] B. Das, B. Balasubramanian, P. Manchanda, P. Mukherjee, R. Skomski, G. C. Hadjipanayis, and D. J. Sellmyer, Nano Lett. 16, 1132 (2016).
- [10] A. F. Rodríguez, A. Kleibert, J. Bansmann, A. Voitkans, L. J. Heyderman, and F. Nolting, Phys. Rev. Lett. 104, 127201 (2010).
- [11] A. Hillion, A. Cavallin, S. Vlaic, A. Tamion, F. Tournus, G. Khadra, J. Dreiser, C. Piamonteze, F. Nolting, S. Rusponi, K. Sato, T. J. Konno, O. Proux, V. Dupuis, and H. Brune, Phys. Rev. Lett. 110, 087207 (2013).
- [12] S. M. Stishov, A. E. Petrova, V. A. Sidorov, and D. Menzel, Phys. Rev. B 86, 064433 (2012).
- [13] L. Liao, Y.-C. Lin, M. Bao, R. Cheng, J. Bai, Y. Liu, Y. Qu, K. L. Wang, Y. Huang, and X. Duan, Nature (London) 467, 305 (2010)
- [14] C.-.J. Chiou, S.-P. Chiu, J.-J. Lin, and Y.-C. Chou, Cryst. Eng. 17, 4276 (2015).
- [15] B. Balasubramanian, P. Manchanda, R. Pahari, Z. Chen, W. Zhang, S. R. Valloppilly, X. Li, A. Sarella, L. Yue, A. Ullah,

- P. Dev, D. A. Muller, R. Skomski, G. C. Hadjipanayis, and D. J. Sellmyer, Phys. Rev. Lett. **124**, 057201 (2020).
- [16] B. Balasubramanian, P. Manchanda, R. Skomski, P. Mukherjee, S. R. Valloppilly, B. Das, G. C. Hadjipanayis, and D. J. Sellmyer, Appl. Phys. Lett. 108, 152406 (2016).
- [17] Z. Rao, H. Li, T. Zhang, S. Tian, C. Li, B. Fu, C. Tang, L. Wang, Z. Li, W. Fan, J. Li, Y. Huang, Z. Liu, Y. Long, C. Fang, H. Weng, Y. Shi, H. Lei, Y. Sun, T. Qian, and H. Ding, Nature (London) 567, 496 (2019).
- [18] D. S. Sanchez, I. Belopolski, T. A. Cochran, X. Xu, J.-X. Yin, G. Chang, W. Xie, K. Manna, V. Süß, C.-Y. Huang, N. Alidoust, D. Multer, S. S. Zhang, N. Shumiya, X. Wang, G.-Q. Wang, T.-R. Chang, C. Felser, S.-Y. Xu, S. Jia *et al.*, Nature (London) **567**, 500 (2019).
- [19] G. Liu, Y.-C. Lin, L. Liao, L. Liu, Y. Chen, Y. Liu, N. O. Weiss, H. Zhou, Y. Huang, and X. Duan, Nano Lett. 12, 1972 (2012).
- [20] K. Seo, S. Lee, H. Yoon, J. In, K. S. K. Varadwaj, Y. Jo, M.-H. Jung, J. Kim, and B. Kim, ACS Nano 3, 1145 (2009).
- [21] C. Bormio-Nunes, C. Angelo Nunes, A. A. Coelho, M. I. S. T. Faria, P. A. Suzuki, and G. C. Coelho, J. Alloys Compd. 508, 5 (2010).
- [22] B. Balasubramanian, P. Manchanda, R. Skomski, P. Mukherjee, B. Das, T. A. George, G. C. Hadjipanayis, and D. J. Sellmyer, Appl. Phys. Lett. 106, 242401 (2015).
- [23] W. Jones and N. H. March, *Theoretical Solid State Physics I* (Wiley & Sons, London, 1973).
- [24] R. Skomski, B. Balamurugan, P. Manchanda, M. Chipara, and D. J. Sellmyer, IEEE Trans. Magn. 53, 1 (2017).
- [25] ICDD 2014, International Centre for Diffraction Data, Card No. 04-003-2126.
- [26] J. M. Yeomans, *Statistical Mechanics of Phase Transitions* (Oxford University Press, Oxford, 1992).
- [27] P. Mohn, Magnetism in the Solid State (Springer, Berlin, 2003).
- [28] P. Fulde, *Electron Correlations in Molecules and Solids* (Springer, Berlin, 1991).

- [29] E. P. Wohlfarth, J. Appl. Phys. 39, 1061 (1968).
- [30] S. Foner and E. J. McNiff, Phys. Rev. Lett. 19, 1438 (1967).
- [31] See Supplemental Material at http://link.aps.org/supplemental/ 10.1103/PhysRevMaterials.5.024402 for additional details on methods, structure, and magnetic and electron-transport properties.
- [32] S. Chikazumi, *Physics of Magnetism* (Wiley, New York, 1964).
- [33] G. Hadjipanayis, D. J. Sellmyer, and B. Brandt, Phys. Rev. B 23, 3349 (1981).
- [34] P. M. H. Danan and R. Barbier, J. Phys. Radium 21, 822 (1960).
- [35] A. Franco, Jr., and F. C. e Silva, Appl. Phys. Lett. 96, 172505 (2010).
- [36] R. Skomski, Simple Models of Magnetism (Oxford University Press, Oxford, 2008).
- [37] G. Kresse and J. Furthmüller, Phys. Rev. B **54**, 11169 (1996).
- [38] J. P. Perdew, K. Burke, and M. Ernzerhof, Phys. Rev. Lett. 77, 3865 (1996).
- [39] K. L. Pisane, S. Singh, and M. S. Seehra, Appl. Phys. Lett. 110, 222409 (2017).
- [40] P. Gambardella, S. Rusponi, M. Veronese, S. S. Dhesi, C. Grazioli, A. Dallmeyer, I. Cabria, R. Zeller, P. H. Dederichs, K. Kern, C. Carbone, and H. Brune, Science 300, 1130 (2003).
- [41] R. Skomski, J. Phys.: Condens. Matter 15, R841 (2003).
- [42] Y. Qu, J. Bai, L. Liao, R. Cheng, Y.-C. Lin, Y. Huang, T. Guod, and X. Duan, Chem. Commun. 47, 1255 (2011).
- [43] A. Kolodziejczyk and J. Spalek, J. Phys. F: Metal Phys. 14, 1277 (1984).
- [44] H. Yamada and S. Takada, Prog. Theor. Phys. 48, 1828 (1972).
- [45] P. Kharel, R. Skomski, P. Lukashev, R. Sabirianov, and D. J. Sellmyer, Phys. Rev. B 84, 014431 (2011).
- [46] C. Kim, W. Yoo, H.-W. Bang, S. Lee, Y. C. Park, Y. H. Lee, J. Choi, Y. Jo, K. Lee, and M.-H. Jun, ACS Omega 4, 16578 (2019)
- [47] L. J. Zhu, S. H. Nie, P. Xiong, P. Schlottmann, and J. H. Zhao, Nat. Commun. 7, 10817 (2016).
- [48] Y. M. Lu, J. W. Cai, Z. Guo, and X. X. Zhang, Phys. Rev. B **87**, 094405 (2013).
- [49] C. Wang, C.-H. Chang, A. Huang, P.-C. Wang, P.-C. Wu, L. Yang, C. Xu, P. Pandey, M. Zeng, R. Böttger, H.-T. Jeng, Y.-J. Zeng, M. Helm, Y.-H. Chu, R. Ganesh, and S. Zhou, Phys. Rev. Materials 3, 053801 (2019).

- [50] J. M. D. Coey, A. E. Berkowitz, Ll. Balcells, F. F. Putris, and A. Barry, Phys. Rev. Lett. 80, 3815 (1998).
- [51] N. V. Dalakova, B. I. Belevtsev, E. Yu. Beliayev, A. N. Bludov, and V. N. Pashchenko, Low Temp. Phys. 38, 1121 (2012).
- [52] V. O. Golub, V. A. Chernenko, A. Apolinario, I. R. Aseguinolaza, J. P. Araujo, O. Salyuk, J. M. Barandiaran, and G. N. Kakazei. Sci. Rep. 8, 15730 (2018).
- [53] C. Sürgers, G. Fischer, P. Winkel, and H. v. Löhneysen, Nat. Commun. 5, 3400 (2014).
- [54] W. J. Xu, B. Zhang, Z. X. Liu, Z. Wang, W. Li, Z. B. Wu, R. H. Yu, and X. X. Zhang, Europhys. Lett. 90, 27004 (2007).
- [55] I. Rosenman and F. Batallan, Phys. Rev. B 5, 1340 (1972).
- [56] Y. Tian, L. Ye, and X. Jin, Phys. Rev. Lett, 103, 087206 (2009).
- [57] D. Destraz, L. Das, S. S. Tsirkin, Y. Xu, T. Neupert, J. Chang, A. Schilling, A. G. Grushin, J. Kohlbrecher, L. Keller, P. Puphal, E. Pomjakushina, and J. S. White, npj Quantum Mater. 5, 1 (2020).
- [58] T. Golod, A. Rydh, P. Svedlindh, and V. M. Krasnov, Phys. Rev. B 87, 104407 (2013).
- [59] D. Hou, Y. Li, D. Wei, D. Tian, L. Wu, and X. Jin, J. Phys.: Condens. Matter 24, 482001 (2012).
- [60] J. Kötzler and W. Gil, Phys. Rev. B 72, 060412(R) (2005).
- [61] Q. Wang, Y. Xu, R. Lou, Z. Liu, M. Li, Y. Huang, D. Shen, H. Weng, S. Wang, and H. Lei, Nat. Commun. 9, 3681 (2018).
- [62] S. X. Huang and C. L. Chien, Phys. Rev. Lett. 108, 267201 (2012).
- [63] S. Onoda, N. Sugimoto, and N. Nagaosa, Phys. Rev. B 77, 165103 (2008).
- [64] S.-Y. Yang, Y. Wang, B. R. Ortiz, D. Liu, J. Gayles, E. Derunova, R. Gonzalez-Hernandez, L. Šmejkal, Y. Chen, S. S. P. Parkin, S. D. Wilson, E. S. Toberer, T. McQueen, and M. N. Ali, Sci. Adv. 6, eabb6003 (2020).
- [65] L. Ye, Y. Tian, X. Jin, and D. Xiao, Phys. Rev. B 85, 220403(R) (2012).
- [66] K. Uenoa, T. Fukumura, H. Toyosaki, M. Nakano, and M. Kawasaki, Appl. Phys. Lett. 90, 072103 (2007).
- [67] Y. Shiomi, Y. Onose, and Y. Tokura, Phys. Rev. B 79, 100404(R) (2009).
- [68] T. Miyasato, N. Abe, T. Fujii, A. Asamitsu, S. Onoda, Y. Onose, N. Nagaosa, and Y. Tokura, Phys. Rev. Lett. 99, 086602 (2007).